International Journal of Heat and Mass Transfer 52 (2009) 3137–3146

Contents lists available at ScienceDirect

International Journal of Heat and Mass Transfer

journal homepage: www.elsevier.com/locate/ijhmt

# Numerical simulation of laser irradiation to a randomly packed bimodal powder bed

Jianhua Zhou, Yuwen Zhang *, J.K. Chen

*Department of Mechanical and Aerospace Engineering, University of Missouri, Columbia, MO 65211, USA*

ARTICLE INFO

*Article history:*
Received 4 April 2008
Received in revised form 29 January 2009
Accepted 29 January 2009
Available online 21 March 2009

*Keywords:*
Selective laser sintering
Laser irradiation
Radiative transfer
Random packing
Ray tracing method

ABSTRACT

Bimodal packing arrangements can be used to overcome the balling phenomena in selective laser sintering (SLS). However, little attention has been paid to the effects of bimodal packing structures on radiative transfer in the SLS powder beds. In this study, a sequential addition packing algorithm is firstly employed to generate 3-D random packing of opaque, diffusively or specularly reflecting spherical particles with the same or different sizes. Then, a Monte Carlo based ray tracing algorithm is formulated, for the first time, to simulate the radiative transfer in the bimodal random packing structures composed of particles with different sizes and emissivities. The credibility of the computer code is verified with published experimental data. A comparison is also made between the calculating results and those obtained by two-flux model. By using the present algorithm, the radiative heat fluxes at both levels of particle and entire bed as well as the transmitted laser energy are statistically evaluated. The influences of bimodal size distribution and particle surface emissivity on the radiative transfer process are examined. Such information is expected to be helpful for optimizing the SLS process.



## 1. Introduction

Selective laser sintering (SLS) is an emerging technology that can fabricate structurally sound parts from powdered materials using a directed laser beam [1]. It is an efficient and rapid technique for manufacturing complex parts that are often unobtainable by conventional manufacturing processes [2,3]. One obstacle of the SLS process is the balling phenomenon, in which melted powder grains stick to each other due to the surface tension force, thereby forming a series of spheres with diameters approximately equal to the laser beam diameter [2,4]. One way to overcome the balling phenomenon is to use two different types of metal powders, one with a significantly higher melting point than the other [5]. During the SLS process, only the powders with the lower melting point are molten and those with the higher melting point remain in solid. Another new idea recently proposed is to use bimodal powders having the same composition but distinctive sizes [6]. In such a packing process, those smaller particles will be heated up faster than the larger particles because the former have lower thermal inertia. This could lead to melting of the smaller particles in the mixture while the large particles are still in the solid phase.

In SLS processes, the three-dimensional functional parts are created using the layered manufacturing technique by fusing powered materials with a moving laser beam. Melting and resolidification are the mechanisms that bond metal powder particles to form a layer and also bond different layers together to form a functional part. For reaching a desired sintering depth, heat transfer analysis needs to be performed such that laser parameters, such as laser intensity, laser beam radius, laser beam scanning velocity, etc., can be correctly chosen prior to the real SLS procedure. However, modeling the thermal process in SLS is very difficult due to the many different physical processes involved. The liquid flow driven by surface tension and buoyancy forces, the shrinkage phenomena induced by the overall density change, the powder particle motion due to shrinkage effect have been proved to play important roles in the temperature transients and thus the sintering rate and depth. To predict these complex physical processes, one must know the laser energy deposition distribution in the power bed. The thermal behavior and fluid dynamics in such a multiphase system strongly depend on laser energy deposition in the packing bed. Since 3-D random packing structures are an open pore system, laser radiation can penetrate into deep part of the powder beds through multiple reflections from particle surfaces. Understanding and accurately modeling radiative transfer in such packing structures is critical for the subsequent radiation–conduction–convection coupled heat transfer analysis. To date, most of the radiative heat transfer models for packing structures have been developed for powders having the same composition and size (e.g., [7–11]). Little has been done on laser light transport in a packing bed containing powders of different compositions or sizes. Therefore, there is a need for establishing a theoretical model that can predict the radiative transfer in randomly packed beds that contain powder particles having different radiative properties and/or sizes.

The existing theoretical models for simulation of the radiative transfer in packing structures can be classified into two main categories [12]: (1) continuous or pseudo-continuous models and (2) discontinuous or discrete models. For the former, the theories are

* Corresponding author.
*E-mail address:* zhangyu@missouri.edu (Y. Zhang).

0017-9310/$ - see front matter © 2009 Elsevier Ltd. All rights reserved.
doi:10.1016/j.ijheatmasstransfer.2009.01.028

**Nomenclature**

| | |
|---|---|
| $a$, $b$ | effective absorption coefficient and back-scattering coefficient, $m^{-1}$ |
| $i^+$, $i^-$ | forward and backward radiant intensities in two-flux model, $W/m^2$ |
| $\mathbf{i}$, $\mathbf{j}$, $\mathbf{k}$ | unit vectors in the $x$, $y$, z directions |
| $\mathbf{i}'$, $\mathbf{j}'$, $\mathbf{k}'$ | unit vectors in the $x', y', z'$ directions |
| $i'_x$, $i'_y$, $i'_z$ | scalar components of the unit vector $\mathbf{i}'$ in the $x$, $y$, z directions |
| $j'_x$, $j'_y$, $j'_z$ | scalar components of the unit vector $\mathbf{j}'$ in the $x$, $y$, z directions |
| $k'_x$, $k'_y$, $k'_z$ | scalar components of the unit vector $\mathbf{k}'$ in the $x$, $y$, z directions |
| $n_1$, $n_2$ | numbers of larger and smaller spheres, respectively, m |
| $n_x$, $n_y$, $n_z$ | direction cosines of outward normal of the sphere surface |
| $N_r$ | total simulation number of rays in Monte Carlo simulation |
| $N_t$ | total simulation number of spheres in packing algorithm |
| $P$ | laser incident power, W |
| $r_l$ | radius of laser spot, m |
| $R$ | radius of spherical particle, m |
| $R_1$, $R_2$ | radii of larger and smaller spheres, respectively, m |
| $R_i$ | radius of the $i$th sphere, m |
| $s$ | traveling length of radiation ray, m |
| $S_i$ | total weight of the rays absorbed by the $i$th sphere |
| $S_l$ | total weight of the rays deposited on an surface element of particle |
| $W$ | ray weight |
| $W_r$ | weight of the reflected ray |
| $W_i$ | weight of the incident ray |
| $x$, $y$, $z$ | global reference frame, m |
| $x'$, $y'$, $z'$ | local reference frame for ray reflection on particles, m |
| $x''$, $y''$, $z''$ | local reference frame for ray absorption on particles, m |
| $x_c$, $y_c$, $z_c$ | coordinates of particle center, m |
| $x_i$, $y_i$, $z_i$ | coordinates of interacting point, m |
| $x_0$, $y_0$, $z_0$ | current position of the ray, m |
| $x_{max}$, $y_{max}$, $z_{max}$ | dimensions of the packing container, m |

*Greek symbols*

| | |
|---|---|
| $\varepsilon$ | emissivity |
| $\phi_1$ | angle of incident ray on specularly scattering spheres, rad |
| $\phi'$, $\theta'$ | zenith angle and azimuth angle in the local reference frame ($x'$, $y'$, $z'$), rad |
| $\phi''$, $\theta''$ | zenith angle and azimuth angle in the local reference frame ($x''$, $y''$, $z''$), rad |
| $\mu_{x1}$, $\mu_{y1}$, $\mu_{z1}$ | direction cosines of incident ray |
| $\mu_{x2}$, $\mu_{y2}$, $\mu_{z2}$ | direction cosines of reflected ray |
| $\mu_x$, $\mu_y$, $\mu_z$ | direction cosines in global reference frame ($x$, $y$, $z$) |
| $\mu'_x$, $\mu'_y$, $\mu'_z$ | direction cosines in local reference frame ($x'$, $y'$, $z'$) |
| $\rho$ | surface reflectivity of particle |
| $\tau$ | transmittance |
| $\xi_i$ | random numbers between 0 and 1 ($i$ = 1, 2, 3, 4) |
| $\Delta\phi''$, $\Delta\theta''$ | angles used to describe the surface element, rad |

developed based on dependent and independent scattering and their applicability limits are demarcated (e.g., [13,14]). For the latter, Monte Carlo and/or ray tracing methods are often used for effectively taking into account the dependent scattering since they are a particle-level simulation technique that can model multiple reflections among particles [15–20]. The authors of Ref. [19] suggested that the Monte Carlo approach is valid if the radius of particle is greater than $\beta\lambda/(2\pi)$, where $\lambda$ is wavelength and $\beta$ is a constant equal to 115. They further suggested the radius are particles should be greater than 75 μm for thermal (infrared) radiation, which corresponds to $\lambda$ = 4 μm. For SLS of metal particles, Nd:YAG laser ($\lambda$ = 1.06 μm) is generally used for better coupling between laser and metal. In this case, the minimum radius that Monte Carlo approach can be used is 19.4 μm. The radius of particles that is commonly used in SLS is generally greater than this limit, which makes Monte Carlo approach an ideal tool to simulate laser interaction with powder particles for most SLS applications.

In this study, a sequential addition packing algorithm is employed to generate 3-D randomly packed structures that are composed of spherical particles with the same or different sizes. A Monte Carlo based ray tracing scheme is then established to simulate the radiative transfer in the bimodal random packing structures. The computer code is validated by comparison with existing experimental data. The results are also compared to those obtained by two-flux model. Using the present algorithm, important radiative information, such as radiation heat flux on each particle surface, laser light penetration in the powder bed, transmitted laser energy, etc., are evaluated and discussed.

## 2. Theoretical consideration

The radiant intensity through a slab of packed powders is attenuated by particle absorption and scattering, and is augmented by particle emission. Two-flux model [21] is a simple but efficient approximation to describe the radiant energy distribution in a 1-D medium where isotropic scattering is predominant. Two-flux approximation involves the assumption that the intensity at any point can be divided into a forward $i^+$ and a backward $i^-$ component. Assuming no emission, the equation of radiative transfer can be integrated over the forward and the backward directions to give:

$$\frac{di^+}{dl} = -(a+b)i^+ + bi^- \tag{1}$$

$$-\frac{di^-}{dl} = -(a+b)i^- + bi^+ \tag{2}$$

where $l$ is the coordinate in the direction of radiative heat transfer and perpendicular to the boundary plane of the packed beds, $i^+$ and $i^-$ are the radiant intensities in the positive and negative $l$ direction, and $a$ and $b$ are the effective absorption coefficient and back-scattering coefficient.

As shown by Kubelka [22], the transmittance $\tau$ of a slab of packed particles having a finite thickness $L$ can be found by solving the two-flux equations with boundary conditions:

$$i^+ = i_0 \quad l = 0 \tag{3}$$

$$i^- = 0 \quad l = L \tag{4}$$

The transmittance is:

$$\tau = \frac{\sqrt{a(a+2b)}}{\sqrt{a(a+2b)}\cosh(L\sqrt{a(a+2b)}) + (a+b)\sinh(L\sqrt{a(a+2b)})} \tag{5}$$

## 3. Numerical model description

The Monte Carlo based ray tracing method is a particle-level simulation technique, requiring the detailed powder packing structure by particle locations and sizes, population ratio, coordination

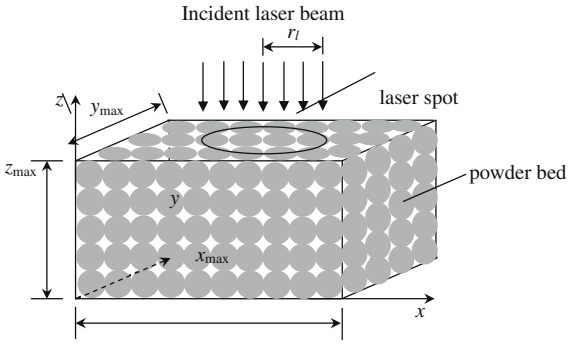


**Fig. 1.** Schematic of the configuration of a powder bed.

number, etc. In this study, the sequential addition algorithm [23–25] is employed to simulate the 3-D random packing process of different-size spherical particles. Although the packed beds, obtained using the random packing algorithm described in Section 2.1, should be irregular, a regular packing structure of dimensions $x_{max} \times y_{max} \times z_{max}$ is sketched in Fig. 1 for ease of explanation.

### 3.1. 3-D random packing algorithm

The sequential addition packing simulation starts with dropping a randomly chosen spherical particle, according to a pre-generated particle size distribution, into a $x_{max} \times y_{max} \times z_{max}$ rectangular container. The final positions of the incoming spheres are decided by the dropping and rolling rules that are devised from the physical process of spheres dropping in the gravitational field by minimizing its gravity potential. Initially, spheres at coordinates $(x, y, z)$ are allocated (Fig. 1), where $(x, y)$ are chosen randomly and $z$ is well above the top of the defined container. Each sphere moves down along a vertical path (i.e., constant $x$ and $y$ with varying $z$) until its surface contacts with a deposited sphere or hits the floor of the container. If it hits the floor, its final position is determined. Otherwise, the following rolling rule is applied: the sphere rolls down in a vertical plane along its contacting sphere surface until it contacts with another sphere.

When a falling sphere is in contact with two deposited spheres, it is at an unstable state and its gravity potential has to be reduced further. Thus, the sphere will keep on rolling downwards with the double contacts until it hits a third particle or the floor. Whether it becomes stable or not is determined by a stabilization judgment based on the criterion of minimum gravitational potential. If stable, the current location is the final position of the sphere. Then, the model will turn to generate another new sphere. Otherwise, it continues to roll down. The periodic boundary condition is applied to eliminate the wall effects. Any sphere that leaves the container through a vertical wall or a corner will immediately reenter the opposite wall or corner. The details of the algorithm of particle rolling down, the stabilization judgment, and the computer program flow chart are described in the authors' previous work [25].

### 3.2. Monte Carlo ray tracing procedure

Instead of performing the simulation for a representative unit cell, a full Monte Carlo ray tracing approach is employed to evaluate the radiative transfer throughout the entire medium in this study. Consider a packing structure of dimensions $x_{max} \times y_{max} \times z_{max}$ (Fig. 1). A flat-top, continuous-wave laser beam with a radius of $r_l$ and a total power of $P$ is impinging onto the packed bed. Assume that the center of the laser spot coincides with the center of the upper surface of the packed bed. The global rectangular reference frame *Oxyz* that is fixed to the 3-D packed bed is used to trace the radiation ray movement. Another local reference frame will be introduced to quantify the reflection behavior when a ray hits a particle.

A radiation ray is characterized by its starting point (at the plane $z = z_{max}$), direction and energy (represented by a weight value, initially set to be 1 and decreasing as the ray energy is absorbed by power particles). An interaction is said to occur when a radiation ray hits a particle, and the hitted point is referred to as the interacting point. When a ray first enters the packed bed, a part of its energy is absorbed by the interacted particle and the rest is reflected. The reflected ray may escape from the packed bed, or hit another particle and then repeats the absorption and reflection process. Due to the long pore paths in the packed bed, the reflected ray may undergo multiple interactions. Each ray is traced until all the rays escape from or pass through the packed bed or until the ray's weight is below a prescribed value (e.g., 0.0001).

The starting position of an incident ray can be described by:

$$x = x_{max}/2 + r_l\sqrt{\xi_1}\cos(2\pi\xi_2) \tag{6}$$

$$y = y_{max}/2 + r_l\sqrt{\xi_1}\sin(2\pi\xi_2) \tag{7}$$

$$z = z_{max} \tag{8}$$

where $\xi_1$ and $\xi_2$ are random numbers between 0 and 1. Since the laser incident radiation direction is collimated and perpendicular to the $x$–$y$ plane, the direction cosines of the incident ray are $(0, 0, -1)$. Let the current position of the ray be $(x_0, y_0, z_0)$, the new position $(x, y, z)$ after traveling a length $s$ becomes:

$$x = x_0 + \mu_x s \tag{9}$$

$$y = y_0 + \mu_y s \tag{10}$$

$$z = z_0 + \mu_z s \tag{11}$$

where $\mu_x$, $\mu_y$ and $\mu_z$ are the direction cosines of the reflected ray, determined by the previous interaction condition.

The next interacting point can be obtained by substituting Eqs. (9)–(11) into the equation of the powder sphere

$$(x - x_c)^2 + (y - y_c)^2 + (z - z_c)^2 = R^2 \tag{12}$$

To find the minimum distance $s$, Eq. (12) is solved for all the spheres in the packed bed. The distance that the ray travels before it intersects all the boundary surfaces is also determined. The minimum of all the $s$ solutions gives the new interacting point or the intersection point with a bounding surface. In case a radiation ray passes through the upper or the lower face, the energy associated with the ray is registered as transmission or reflection.

Selective laser sintering can use a number of build materials including: nylon, glass filled nylon, elastomers, waxes, polycarbonates, ceramics, metals, etc. Therefore, the particle surface may be diffusive or specular, depending on which material is employed in the SLS process. For metal powder SLS process, the powders are usually polished ones without surface impurities. The whole SLS process is kept inside a heated chamber filled with an inert gas such as nitrogen to reduce unwanted contamination with the atmosphere. Therefore, it is more reasonable to treat the metal powder surface as being optically specular.

In the following, the direction cosines of the reflected ray on both specularly and diffusively scattering spheres will be derived.

For a specularly scattering sphere, the direction of the reflected ray is found using the laws of reflection, i.e.: (1) the incident ray, the reflected ray and the normal of the surface all lie in the same plane; (2) the angle of incidence is equal to the angle of reflection.

The angle of incidence $\phi_1$, the angle between the incidence direction and the outward normal, is calculated by:

$$\phi_1 = \arccos[-(\mu_{x1}n_x + \mu_{y1}n_y + \mu_{z1}n_z)] \tag{13}$$

where $\mu_{x1}$, $\mu_{y1}$, $\mu_{z1}$ and $n_x$, $n_y$, $n_z$ are the direction cosines of incident ray and outward normal of the sphere surface.

The direction cosines of the reflected ray is computed based on the laws of reflection:

$$\mu_{x2}=\mu_{x1}+2n_x\cos\phi_1;\quad \mu_{y2}=\mu_{y1}+2n_y\cos\phi_1;\mu_{y2}=\mu_{y1}+2n_y\cos\phi_1 \tag{14}$$

The direction cosines of the reflected ray on diffusively scattering spheres are derived as follows. Let $(x', y', z')$ be a local reference frame with its origin coinciding with the center of the interacting sphere and the $z'$-axis pointing to the interacting point. Let $\mathbf{i}'$, $\mathbf{j}'$ and $\mathbf{k}'$ be the unit vectors along the $x'$, $y'$ and $z'$ axes, respectively, and $\mathbf{i}$, $\mathbf{j}$ and $\mathbf{k}$ the unit vectors along the $x$, $y$ and $z$ axes, respectively. The unit vector $\mathbf{i}'$ is the cross product of $\mathbf{k}'$ and $\mathbf{k}$, and consequently, $\mathbf{j}'$ is the cross product of $\mathbf{k}'$ and $\mathbf{i}'$. Mathematically, the unit vectors $\mathbf{i}'$, $\mathbf{j}'$ and $\mathbf{k}'$ are defined as:

$$\mathbf{k}'=\frac{(x_i-x_c)\mathbf{i}+(y_i-y_c)\mathbf{j}+(z_i-z_c)\mathbf{k}}{\sqrt{(x_i-x_c)^2+(y_i-y_c)^2+(z_i-z_c)^2}};\quad \mathbf{i}'=\mathbf{k}'\times\mathbf{k};$$
$$\mathbf{j}'=\mathbf{k}'\times\mathbf{i}' \tag{15}$$

Since the powder is assumed to be diffusively scattering, a radiation ray will be reflected in a random direction from the interacting point toward to the hemisphere outside the spherical powder. The Monte Carlo sampling technique is applied to generate the random reflection direction [26,27]:

$$\phi'=\sin^{-1}(\sqrt{\xi_3});\quad \theta'=2\pi\xi_4 \tag{16}$$

In Eq. (16), $\xi_3$ and $\xi_4$ are random numbers between 0 and 1. The azimuth angle $\theta'$ and the zenith angle $\phi'$ are measured from the $x'$ and $z'$ axis, respectively.

Once the directional angles $\theta'$ and $\phi'$ are determined, the reflection direction cosines $\mu'_x$, $\mu'_y$ and $\mu'_z$ in the local reference frame are obtained by:

$$\mu'_x=\sin\phi'\cos\theta';\quad \mu'_y=\sin\phi'\sin\theta';\quad \mu'_z=\cos\phi' \tag{17}$$

The reflection direction cosines of the reflected ray referred to the global coordinate system can be computed by matrix multiplication:

$$\begin{Bmatrix}\mu_x\\ \mu_y\\ \mu_z\end{Bmatrix}=\begin{bmatrix}i'_x & j'_x & k'_x\\ i'_y & j'_y & k'_y\\ i'_z & j'_z & k'_z\end{bmatrix}\begin{Bmatrix}\mu'_x\\ \mu'_y\\ \mu'_z\end{Bmatrix} \tag{18}$$

where $i'_x$, $i'_y$, $i'_z$ are the scalar components of the unit vector $\mathbf{i}'$; other symbols in the matrix can be understood in the similar way.

The weight of the reflected ray is decremented to

$$W_r=\rho W_i \tag{19}$$

The remaining part, $(1-\rho)W_i$, is absorbed by the interacting sphere. For a gray surface, the reflectivity $\rho$ can be directly computed according to the emissivity, $\rho = 1-\varepsilon$.

In SLS applications, the incident radiation is from the top surface of the packed bed and each particle is in contact with several neighboring particles. Therefore, the heat flux over the interacted particle surface is far from uniform. To determine the heat flux distribution, the surface of each spherical particle is discretized into small elements. Fig. 2 shows the ray energy deposited onto an surface element $\Delta\phi''\times\Delta\theta''$ (shadowed area) at the azimuth angle $\theta''$ and zenith angle $\phi''$. The surface heat flux ($q_l$) in this area is calculated as:

$$q_l=\frac{P\cdot S_l}{N_r\cdot R^2\cdot\Delta\phi''\cdot\sin\Delta\phi''\cdot\theta''} \tag{20}$$

where $P$ is the total incident power; $N_r$ is the total number of the radiation rays; $R$ is the radius of the interacting sphere; $S_l$ is the total weight of the rays deposited on the element area.

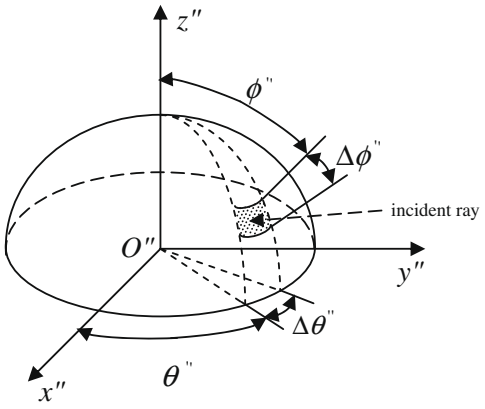


**Fig. 2.** Local reference frame used to describe energy deposition on a single particle surface.

To show the depth dependency of the absorbed radiative flux in the packed bed, the averaged heat flux on each particle surface is computed by

$$q_i=\frac{P\cdot S_i}{N_r\cdot 4\pi R_i^2} \tag{21}$$

where the subscript $i$ denotes the $i$th sphere; $S_i$ and $R_i$ are the total weight of the rays absorbed by and the radius of the sphere, respectively.

## 4. Results and discussions

The parameters that control the quality of a packing structure include packing density and coordination number. The packing density is defined as the total volume of powder spheres divided by the volume of the box containing those spheres. The coordination number is the number of the spheres in contact with a given sphere. The average coordination number is defined as the sum of the coordination numbers of all the spheres divided by the number of the total spheres ($N_t$). The results presented in this paper are non-dimensional or normalized. As mentioned earlier, the Monte Carlo approach is appropriate for Nd:YAG laser ($\lambda = 1.06$ μm) interaction with particles whose radius is greater than 19.4 μm. The radius of particles that is commonly used in SLS is generally greater than this limit, which makes the results presented here valid for most SLS applications. For SLS of particle with smaller size, Maxwell's equation must be solved to obtain the heat flux to the particles.

Fig. 3 shows two typical 3-D random packing structures in a rectangular container, obtained by the present packing algorithm. Fig. 3(a) displays a packed bed that contains equal-size powder spheres. The sphere radius is set as the unit of the dimension. The resulting packing density is 0.57, and the average coordination number is 5.92. Fig. 3(b) shows a different packed bed that is composed of spheres of two different sizes. In this case the radius of the smaller spheres is set as the unit of the dimension, the radius ratio of the larger spheres to the smaller spheres is $R_1/R_2 = 2{:}1$, and the population ratio is $n_1/n_2 = 1{:}1$. The resulting packing density and average coordination number are 0.59 and 5.78, respectively. It is worth noting that the packing density is increased whereas the average coordination number is decreased in comparison with the equal-sized sphere case. This is mainly attributed to the decreasing of average coordination number on the smaller spheres, as seen from the structural analysis in the authors' previous work [25]. The two packing structures shown in Fig. 3 exhibit a good randomicity; no ordered domains are found throughout the packing beds.

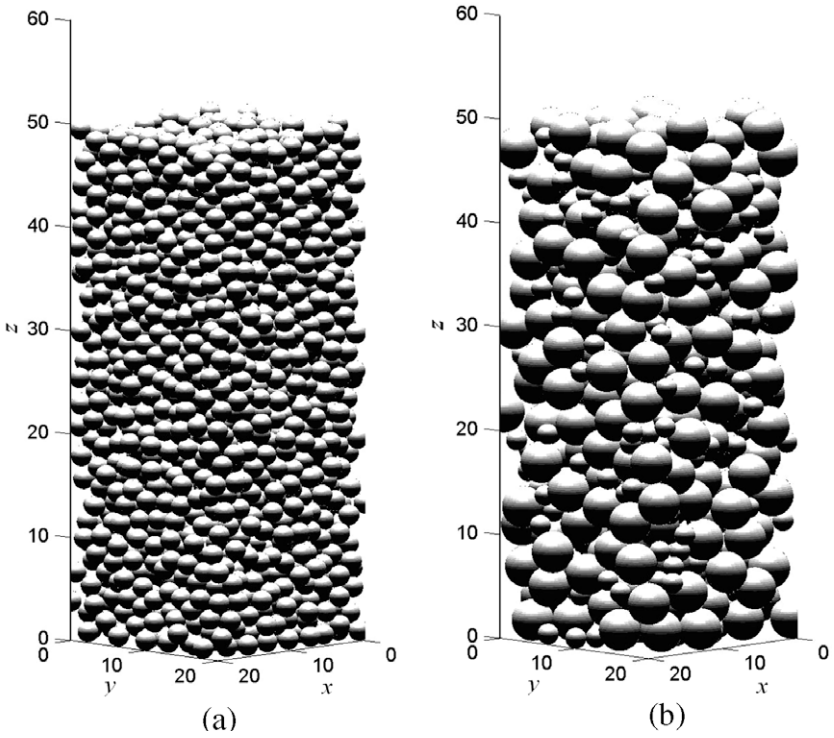


**Fig. 3.** 3-D random packing results: (a) equal-size spheres and (b) different-size spheres.

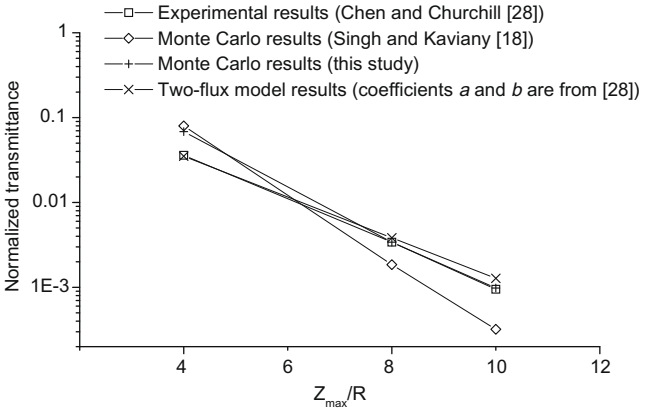


**Fig. 4.** Comparison of normalized transmittance from a packed bed of steel spheres between the present model and the experimental measurement [28].

Fig. 4 compares the transmittance from a packed bed of steel spheres between the modeling results and the experimental measurement. The emissivity of the particle surface taken here is 0.4, as suggested by Chen and Churchill [28]. Since the experimental data [28] is measured for a one-dimensional (1-D) packed bed, the present Monte Carlo simulation is performed based on the 1-D assumption, with which the entire top surface of the packed bed is heated uniformly by a collimated incident flux and the lateral dimensions ($x_{max}$ and $y_{max}$) of the packed bed are much larger than the depth ($z_{max}$). Thus, the starting positions of the incident rays given by Eqs. (6)–(8) are simplified to

$$x = x_{max}\xi_5; \quad y = y_{max}\xi_6; \quad z = z_{max} \tag{22}$$

Our calculation shows that when the lateral dimensions of a packed bed are five times larger than the depth, the change of transmission in lateral directions is negligible, which confirms the adequacy of the 1-D assumption. For consistence with the packing algorithm, the periodic boundary condition is employed in our Monte Carlo simulation. Since the packing powder material is polished carbon steel in the experiments [28], the spherical powder surface is considered to be specular. The normalized transmittance shown in Fig. 4 is obtained by dividing the total weight of the transmitted rays collected at the bottom surface of the packed bed by the total incident ray weight. For comparison, the calculation by Singh and Kaviany [18] and the calculating results obtained by two-flux model are also shown in the figure. The effective absorption and backward scattering coefficients, i.e., $a$ and $b$, are 21.85 $m^{-1}$ and 1213.91 $m^{-1}$, respectively, which are obtained at 1600 °F by Chen and Churchill [28] via experimental data correlation based on the two-flux model. As is seen from Fig. 4, there is a good agreement among the two-flux model results and the Monte Carlo estimations obtained in this study and in Singh and Kaviany's work [18]. Further inspection on Fig. 4 indicates that our calculating results agree better with the experimental data [28] than Singh and Kaviany's results [18]. This may be because Singh and Kaviany used a lower packing density (0.42) in their simulation. The packing density in our simulation is 0.57 which is much closer to 0.60 measured by Chen and Churchill [28].

As mentioned earlier, laser radiation being able to penetrate into deep part of opaque packed particles is due to multiple reflections from the particle surfaces through pore paths. The radiative heat flux distribution on each particle surface needs to be determined prior to the subsequent analysis of melting and sintering heat transfer. Since the present Monte Carlo method is a particle-level technique, the radiative heat flux on each particle surface can be calculated with high accuracy. For example, the coordination number is found to be 5 for the sphere 275 (i.e., the 275th sphere that enters the packing bed) in a packed bed of equal-size spheres and having a total thickness of $z_{max}/R = 8$. Fig. 5(a) shows the sphere and the five contacted particles. The calculated surface heat fluxes as a function of the zenith angle $\phi''$ are presented in Fig. 5(b) for three different azimuth angles $\theta''$, where the heat fluxes are normalized with $P = 1$ and $R = 1$ in

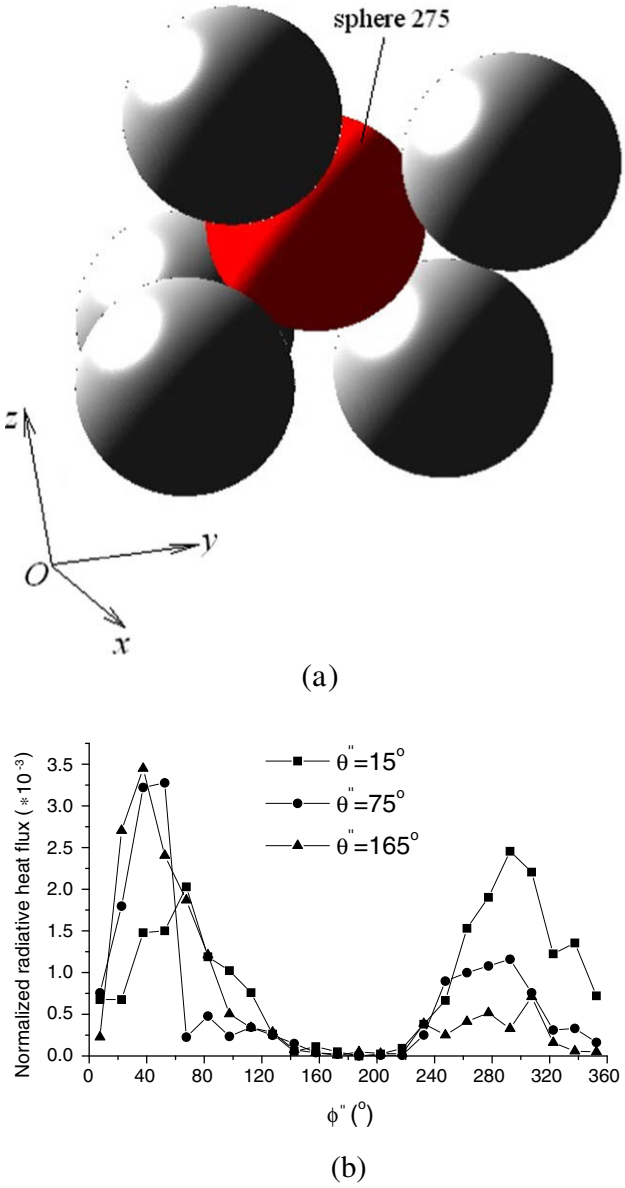


**Fig. 5.** Surface radiative heat flux distribution as a function of azimuth angle $\theta''$ and zenith angle $\phi''$ on a spherical powder in the packed bed.

Eq. (20). The particle surface is treated as specular. As shown in Fig. 5(b), the radiative heat flux varies with $\phi''$ for the same azimuth angle $\theta''$. In addition, the distributions along the zenith angle ($\phi''$) are quite different for different $\theta''$. This indicates that for a randomly packing bed the radiative heat flux distribution on each particle surface is not axisymmetric. Since all the spheres are considered to be opaque, the radiative heat on the surface area near a contacting point must be very small. Thus, the non-uniform distribution of the radiative heat flux is essentially due to the complex contacting condition among particles in a randomly packed bed.

Fig. 6 shows the averaged heat flux (calculated by Eq. (21)) as a function of the bed depth. The simulation conditions used here are identical to those in the previous case shown in Fig. 5. Since the Monte Carlo method is a probability-based technique, the data points are scattered and it would be better to curve fit the simulated results for clarity of presentation. As is seen, the heat flux in the packed bed decreases as the depth increases due to particle absorption.

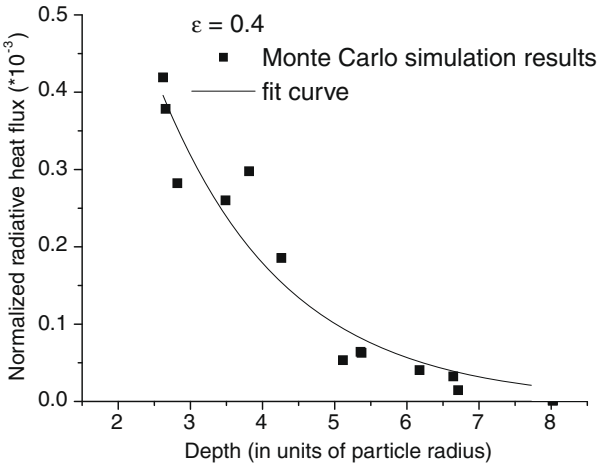


**Fig. 6.** Radiative heat flux distribution over the packed bed depth.

Fig. 7 presents the influence of particle emissivity on the transmittance and reflectance as well as the radiative heat flux distribution over the thickness of the packed bed. The simulation condition is the same as those in Figs. 5 and 6. It can be seen from Fig. 7(a) that the larger the particle emissivity is, the higher the radiative heat flux level can reach. It is also observed from Fig. 7(b) and (c) that both the transmittance and reflectance go down with increase of the powder emissivity.

An efficient way to overcome the balling phenomenon is to pack different types of metal powders that have different melting points and, very probably, have different emissivities. This case is examined in Fig. 8 where the packed bed is composed of powders of two materials with the emissivities of 0.4 and 0.8. The numbers of the two types of powders are assumed to be the same, and so are their radii. The height of the packed bed is eight times larger than the particle radius. The particle surface is optically specular. The two powder components are well mixed since the powders are randomly packed. As shown in Fig. 8(a), the averaged heat flux (the solid curve) falls in between those in the packed beds with powders of one single material ($\varepsilon = 0.4$ or $\varepsilon = 0.8$). Fig. 8(b) and (c) show the surface radiative heat flux distributions on two particles at the same bed height (i.e., the same $z$ coordinate). It is apparent that the radiative flux level on the particle with low emissivity is much smaller than that on the particle with high emissivity. Therefore, to effectively suppress the balling phenomenon, a favorable situation is that those powders with a higher emissivity have a lower melting point so that they can be rapidly molten and sintered with the solid powders that have the opposite properties. The Hagen–Rubens relation [26] shows that the spectral emissivity of pure metals increases with temperature as does the electrical resistivity. However, there is no logical relationship between the emissivity and melting point since the latter is mainly determined by the strength of metal bond. This provides some space for engineers to optimize the SLS manufacturing procedure by choosing a reasonable combination of metal components. Based on our calculating results shown in Fig. 8(b) and (c), it is recommended that preferences be given to those metal pair combinations in which the structural metal has a high melting point and low emissivity whereas the binder metal has a low melting point and high emissivity.

Fig. 9 shows the radiative heat flux results for the packed structures composed of spherical particles with two distinctive sizes. The emissivities of the two groups of particles are identical (0.4), and the thickness of the packed bed is set at $z_{max}/R_2 = 20$ with $R_2$ being the radius of the smaller spheres. In Fig. 9, $R_1/R_2$ represents

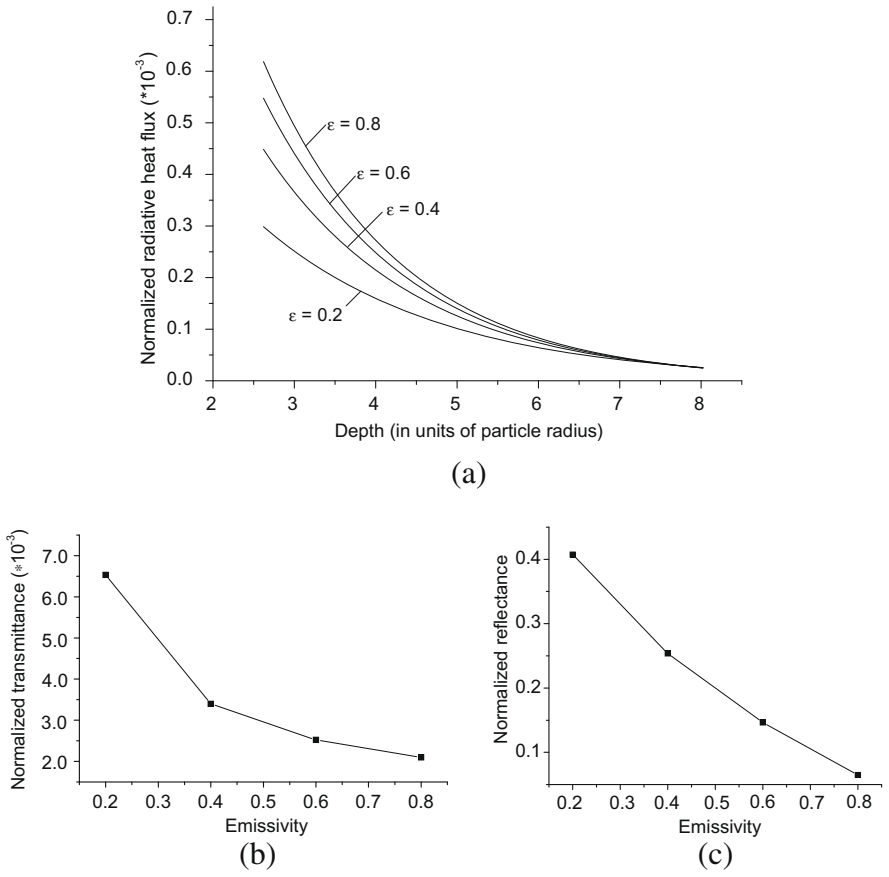


**Fig. 7.** Influence of particle emissivity: (a) radiative heat flux as a function of bed depth, (b) transmittance, and (c) reflectance.

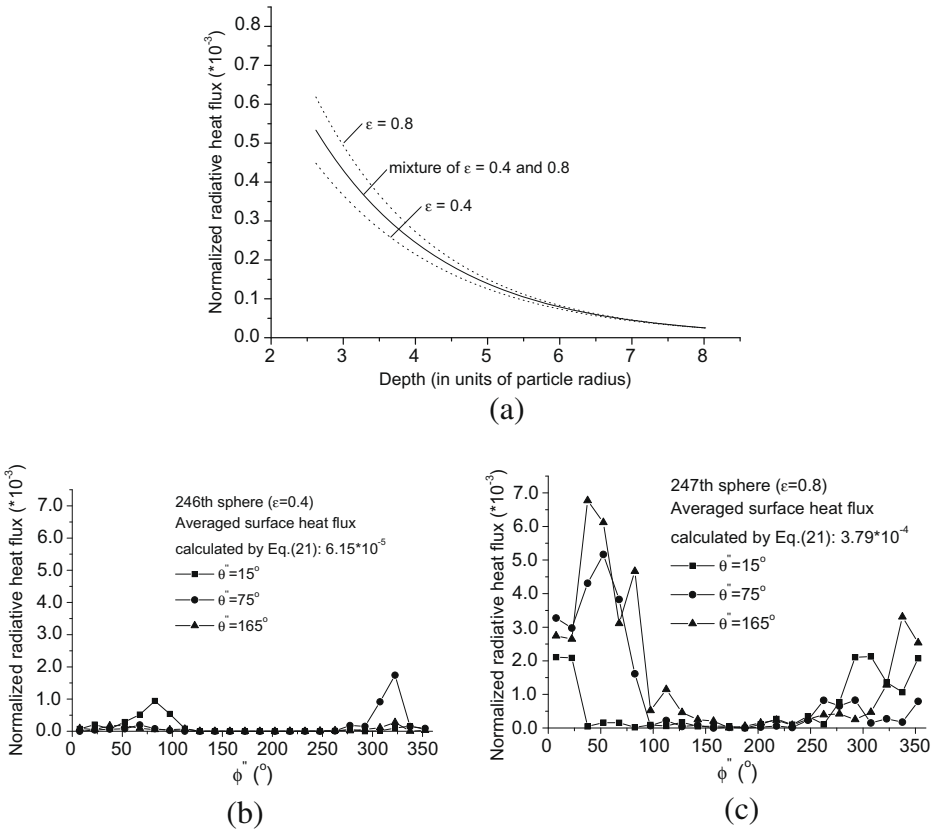


**Fig. 8.** Radiative heat flux in the packed bed composed of particles with different emissivities. (a) Radiative heat flux as a function of bed depth, (b) surface radiative heat flux distribution on particle with low emissivity, and (c) surface radiative heat flux distribution on particle with high emissivity.

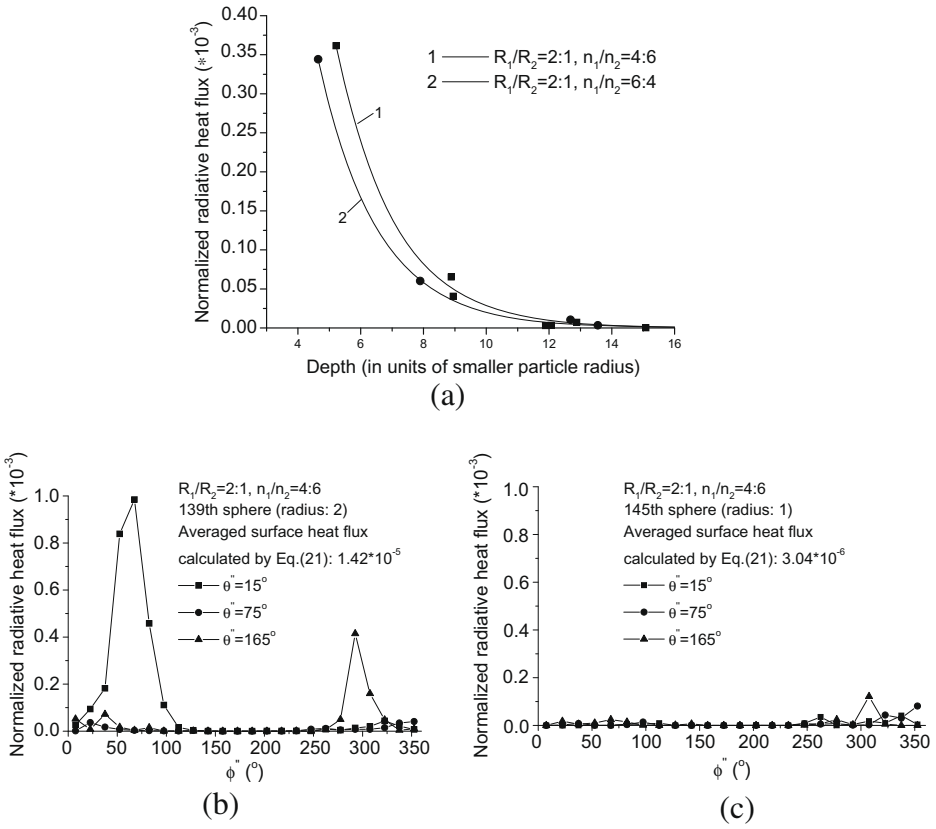


**Fig. 9.** Radiative heat flux in the packed bed composed of particles with different sizes. (a) Radiative heat flux as a function of bed depth, (b) surface radiative heat flux distribution on larger particle for the case $R_1/R_2 = 2{:}1$ and $n_1{:}n_2 = 4{:}6$, and (c) surface radiative heat flux distribution on smaller particle for the case $R_1/R_2 = 2{:}1$ and $n_1{:}n_2 = 4{:}6$.

the radius ratio of the larger particles to the smaller ones, and $n_1/n_2$ denotes their population ratio. The radius of the smaller sphere is set as the unit of the dimension. It can be seen from Fig. 9(a) that the heat flux level for the case $n_1/n_2 = 4{:}6$ is higher than that for the case $n_1/n_2 = 6{:}4$. This indicates that a higher energy flux can be achieved when a bimodal distribution having less larger particles. Fig. 9(b) and (c) show the surface radiative heat flux distributions on two particles at the same bed height for the case $R_1/R_2 = 2{:}1$ and $n_1{:}n_2 = 4{:}6$. The same trends are observed for the case $R_1/R_2 = 2{:}1$ and $n_1{:}n_2 = 6{:}4$, and they are not shown here for brevity. It can be seen that the surface radiative heat flux level on larger particles is higher than that on smaller particles. This is because larger particles have more chance to intercept photons due to their large sizes.

As stated earlier, another idea to suppress the balling phenomenon is to use bimodal powders having the same composition but distinctive sizes. On the one hand, the smaller particles have lower thermal inertia. On the other hand, the radiative heat flux on the surface of smaller particles is less than that on larger particle surface due to their weak ability in photon capturing. The melting of smaller particles does not necessarily precede the melting of larger particles, which depends on the combining effect of thermal inertia and local surface radiative heat flux distribution.

In real SLS applications, the two particle components may have different surface scattering modes (i.e., specular or diffusive). The Monte Carlo ray tracing method proposed in this study can easily handle this situation. Fig. 10 plots the calculating results for the packed beds composed of spherical particles with two distinctive sizes and different surface scattering schemes. As can be seen in Fig. 10, curve 1 almost coincides with curve 2, but there is a notable deviation between curve 3 and curve 1. This indicates that the surface scattering mode of smaller particles has less influence on the overall depth-dependence of radiative heat flux compared to that of the larger particles.

So far, we have discussed the 1-D radiative transfer in laser irradiated packed beds. In practical SLS process, the laser spot size usually is finite and smaller than the lateral dimensions of a powder bed. Fig. 11 shows the calculating results for the finite laser beam case. In this simulation, monosized particle packing is considered. The thickness of the packed bed is $z_{max} = 4$ (the particle radius is set as the unit dimension), and the particle emissivity is $\varepsilon = 0.4$. The powder surface is optically specular. Two sub-cases, stationary

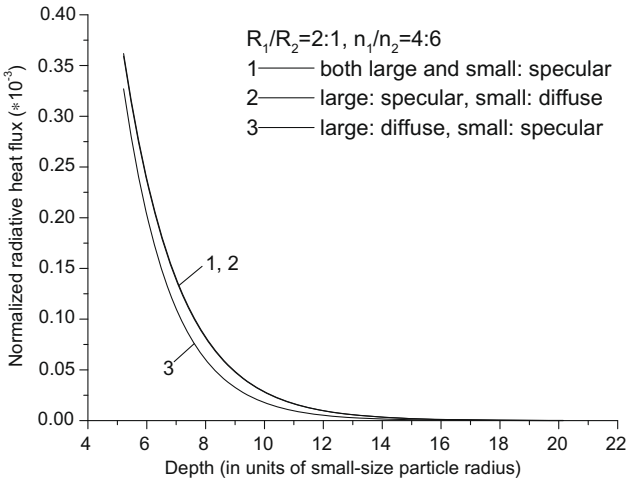


**Fig. 10.** Radiative heat flux changing with depth for the packed beds composed of particles with two distinctive sizes and different surface scattering modes.

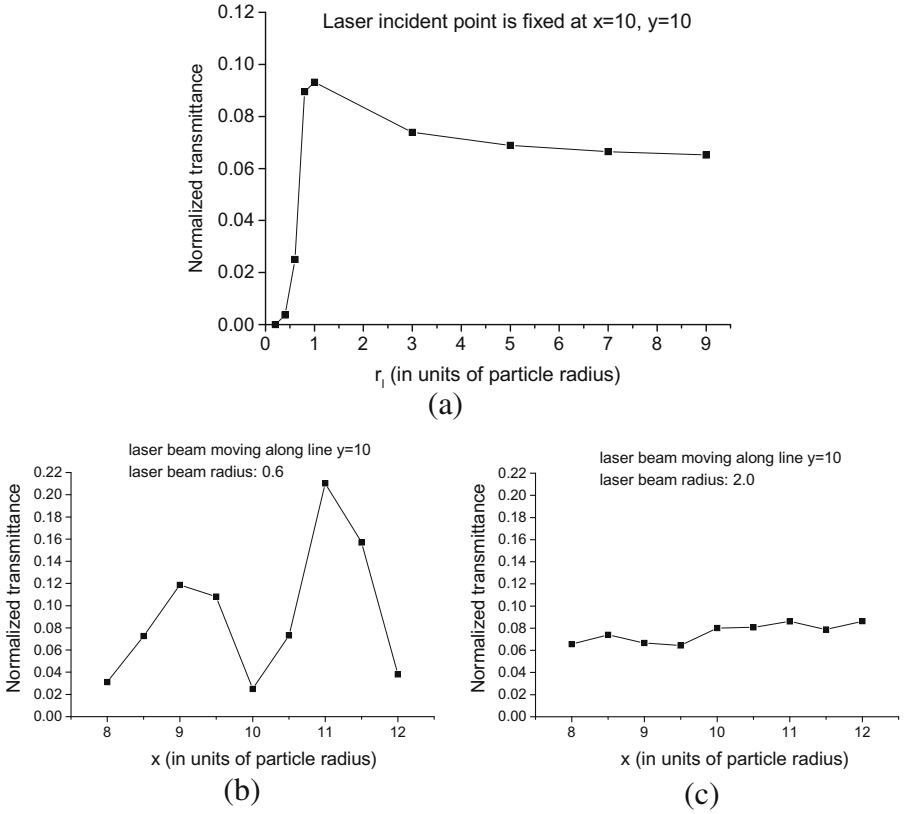


**Fig. 11.** Calculating results for the case of finite laser spot size when the laser incident point is either fixed or moved. (a) Transmittance for stationary laser beam, (b) transmittance for moving laser beam along the line $y = 10$ ($r_l = 0.6$), and (c) transmittance for moving laser beam along the line $y = 10$ ($r_l = 2.0$).

beam and moving beam, are examined. Fig. 11(a) shows the effect of laser spot size on transmittance when the laser incident point is fixed at $x = 10$, $y = 10$. As shown in Fig. 11(a), transmittance signal drastically increases in the region $0 < r_l < 1$, then reaches a peak value at around $r_l = 1$, and eventually approaches a saturated value. Fig. 11(b) and (c) show the transmittance results for moving laser beam case, which corresponds to the single-line laser scanning SLS procedure. As can be seen, when the laser beam radius is 0.6 (Fig. 11(b)), there is a severe fluctuation in the transmittance signal during the laser beam scanning process. However, when the laser beam radius is increased to 2.0, the transmittance signal is quite stable during the beam moving process. The fluctuation in Fig. 11(b) is essentially caused by the random nature of the packing structure, which is an open pore system. Varying local porosities in such a system lead to different penetration ability of laser beam. However, the effect of the random nature of the packing system on the penetration depth will be offset by increasing the laser beam size.

## 5. Conclusions

In this study, a sequential addition packing algorithm is employed to generate 3-D random packing of spherical particles with the same or different sizes. Then, a Monte Carlo based ray tracing algorithm is formulated to simulate the radiation heat transfer in the bimodal random packing structures. After the credibility of the Monte Carlo computer code is verified with previously published experimental and numerical results, the radiative transfer characteristics of bimodal packing structures are investigated. The influences of particle surface emissivity and population ratio of larger particles to smaller particles on the radiative transfer process are examined. Non-uniform radiative heat flux distribution on an individual sphere is demonstrated and analyzed. It is found that a bimodal packing structure, in which larger particles are less than smaller particles, can achieve a higher radiative heat flux level in the packed bed. To effectively suppress the balling phenomenon, care should be used in choosing the material combination in two-component selective laser sintering. Our calculating results show that preferences should be given to those metal pair combinations in which the structural metal has a high melting point and low emissivity whereas the binder metal has a low melting point and high emissivity. The surface scattering mode of larger particles can significantly affect the radiative heat flux distribution across the bed depth. The effects of stationary and moving laser beams are also examined. The theoretical model and numerical algorithm formulated in this study are the first step aiming at establishing a powerful particle-level heat transfer model for the SLS manufacturing process.

## Acknowledgement

Support for this work by the U.S. National Science Foundation under Grant No. CBET-0730143 is gratefully acknowledged.

## References

[1] J.-P. Kruth, Rapid prototyping – a new application of physical and chemical process for material accretion manufacturing, in: Proceedings of the 11th International Symposium for Electromachining, Lausanne, 1995, pp. 3–28.
[2] M. Agarwala, D. Bourell, J. Beaman, H. Marcus, J. Barlow, Direct selective laser sintering of metals, Rapid Prototyping J. 1 (1995) 26–36.
[3] S. Das, J. Beaman, M. Wohlert, D. Bourell, Direct laser freeform fabrication of high performance metal components, Rapid Prototyping J. 4 (1998) 112–117.
[4] N.K. Tolochko, S.E. Mozzharov, I.A. Yadroitsev, T. Laoui, L. Froyen, V.I. Titov, M.B. Ignatiev, Balling processes during selective laser treatment of powders, Rapid Prototyping J. 10 (2004) 78–87.

[5] D.E. Bunnell, Fundamentals of selective laser sintering of metals. Ph.D. dissertation, University of Texas at Austin, Austin, TX, 1995.
[6] C. Konrad, Y. Zhang, Y. Shi, Melting and resolidification of subcooled metal powder particle subjected to nanosecond laser heating, Int. J. Heat Mass Transfer 50 (11–12) (2007) 2236–2245.
[7] D. Vertmeyer, Radiation in packed solids, in: Proceedings of the Sixth International Heat Transfer Conference, Toronto, vol. 6, 1978, pp. 525–539.
[8] M. Kaviany, Principles of Heat Transfer in Porous Media, Springer-Verlag, New York, 1995.
[9] B.P. Singh, M. Kaviany, Effect of solid conductivity on radiative heat transfer in packed beds, Int. J. Heat Mass Transfer 37 (16) (1994) 2579–2583.
[10] A.K.C. Wu, S.H.K. Lee, Multiple-rays tracing technique for radiative exchange within packed beds, Numer. Heat Transfer B 37 (2000) 469–487.
[11] R. Coquard, D. Baillis, Radiative characteristics of opaque spherical particles beds: a new method of prediction, AIAA J. Thermophys. Heat Transfer 18 (2) (2004) 178–186.
[12] C.L. Tien, Thermal radiation in packed and fluidized beds, ASME J. Heat Transfer 110 (1988) 1230–1242.
[13] B.L. Drolen, C.L. Tien, Independent and dependent scattering in packed-sphere systems, AIAA J. Thermophys. Heat Transfer 1 (1987) 63–68.
[14] R. Coquard, D. Baillis, Radiative characteristics of beds of spheres containing an absorbing and scattering medium, AIAA J. Thermophys. Heat Transfer 19 (2) (2005) 226–234.
[15] C.K. Chan, C.L. Tien, Radiative transfer in packed spheres, ASME J. Heat Transfer 96 (1974) 52–58.
[16] Y.S. Yang, J.R. Howell, D.E. Klein, Radiative heat transfer through a randomly packed bed of spheres by the Monte Carlo method, ASME J. Heat Transfer 105 (1983) 325–332.
[17] K. Kudo, W.J. Yang, H. Tanaguchi, H. Hayasaka, Radiative heat transfer in packed spheres by Monte Carlo method, in: Heat Transfer in High Technology and Power Engineering, Hemisphere, New York, 1987, pp. 529–540.
[18] B.P. Singh, M. Kaviany, Independent theory versus direct simulation of radiation heat transfer in packed beds, Int. J. Heat Mass Transfer 34 (11) (1991) 2869–2882.
[19] C. Argento, D. Bouvard, A ray tracing method for evaluating the radiative heat transfer in porous media, Int. J. Heat Mass Transfer 39 (15) (1996) 3175–3180.
[20] E. Nisipeanu, P.D. Jones, Comparison of Monte Carlo surface exchange with radiative continuum results in large particle dispersions, ASME J. Heat Transfer 122 (2000) 503–508.
[21] A. Schuster, Radiation through a foggy atmosphere, Astrophys. J. 21 (1905) 1–22.
[22] P. Kubelka, New contributions to the optics of intensely light scattering materials: Part I, J. Opt. Soc. Am. 38 (1948) 448–457.
[23] W.M. Visscher, M. Bolsterli, Random packing of equal and unequal spheres in two and three dimensions, Nature 329 (1972) 504–507.
[24] W.S. Jodrey, E.M. Tory, Simulation of random packing of spheres, Simulation 32 (1979) 1–12.
[25] J. Zhou, Y. Zhang, J.K. Chen, Numerical simulation of random packing of spherical particles for selective laser sintering applications, in: Proceedings of the International Mechanical Engineering Congress and Exposition, Boston, MA, 2008, IMECE2008-67856.
[26] R. Siegel, J.R. Howell, Thermal Radiation Heat Transfer, third ed., Hemisphere, Washington, DC, 1992.
[27] M.F. Modest, Radiative Heat Transfer, McGraw-Hill, New York, 1993.
[28] J.C. Chen, S.W. Churchill, Radiant heat transfer in packed beds, AIChE J. 9 (1963) 35–41.